Symmetric Positive Semi-Definite Cartesian Tensor Fiber Orientation Distributions (CT-FOD)

Yonas T. Weldeselassie[a,*], Angelos Barmpoutis[b], M. Stella Atkins[a]

[a] *Medical Image Analysis Lab, School of Computing Science, Simon Fraser University; 8888 University Drive, Burnaby BC, V5A 1S6, Canada*
[b] *Dept. of Computer & Information Science and Engineering, University of Florida; P.O. Box 116120, Gainesville, FL 32611-6120, USA*

Abstract

A novel method for estimating a field of fiber orientation distribution (FOD) based on signal de-convolution from a given set of diffusion weighted magnetic resonance (DW-MR) images is presented. We model the FOD by higher order Cartesian tensor basis using a parametrization that explicitly enforces the positive semi-definite property to the computed FOD. The computed Cartesian tensors, dubbed Cartesian Tensor-FOD (CT-FOD), are symmetric positive semi-definite tensors whose coefficients can be efficiently estimated by solving a linear system with non-negative constraints. Next, we show how to use our method for converting higher-order diffusion tensors to CT-FODs, which is an essential task since the maxima of higher-order tensors do not correspond to the underlying fiber orientations. Finally, we propose a diffusion anisotropy index computed directly from CT-FODs using higher order tensor distance measures thus consolidating the whole analysis pipeline of diffusion imaging solely using CT-FODs. We evaluate our method qualitatively and quantitatively using simulated DW-MR images, phantom images, and human brain real dataset. The results conclusively demonstrate the superiority of the proposed technique over several existing multi-fiber reconstruction methods.

Keywords: diffusion tensor imaging, higher order tensors, fiber orientation distribution functions, anisotropy measures

1. Introduction

Diffusion tensor magnetic resonance imaging (DT-MRI) is a non-invasive imaging technique that measures the self-diffusion of water molecules in the body, thus capturing the microstructure of the underlying tissues. Second order symmetric positive definite (SPD) tensors have commonly been used to model the diffusivity profile at each voxel with the assumption of a single coherent fiber tract per voxel. Under this assumption diffusivity in the direction $\mathbf{g}$ was defined as

$$d(\mathbf{g}) = \mathbf{g}^T \mathbf{D}\, \mathbf{g} \tag{1}$$

where $\mathbf{g} = (g_1, g_2, g_3)^T$ is the diffusion weighting magnetic gradient vector and $\mathbf{D}$ is the 2^{nd} order SPD tensor to be estimated from a set of diffusion weighted magnetic resonance (DW-MR) images. This model, despite its simplicity and robustness, has been shown to be incorrect in regions containing intra-voxel orientational heterogeneity such as crossing and merging of fiber bundles (Aganj et al., 2010; Alexander et al., 2002; Descoteaux et al., 2006, 2007; Tuch et al., 1999, 2003).

Several methods have been proposed to overcome the single fiber orientation limitation of second order tensors. In (Tuch et al., 1999), Tuch et al. proposed the use of diffusion imaging with diffusion weighting gradients applied along many directions distributed almost isotropically on the surface of the unit sphere, a method known as high

*Corresponding author.
Email address: yonas@cs.sfu.ca, 8888 University Drive, Burnaby BC, V5A 1S6, Canada, Tel. +1.778.782.5509, Fax. +1.778.782.3045 (Yonas T. Weldeselassie)

angular resolution diffusion imaging (HARDI). In contrast to rank 2 tensors, this method does not assume any a priori knowledge about the diffusivity profile. A number of approaches have been proposed to compute the ensemble-average diffusion propagator P(r, t) of HARDI data. These methods include q-ball imaging (QBI) (Tuch, 2004), diffusion spectrum imaging (DSI) (Wedeen et al., 2005), and diffusion orientation transform (DOT) (Özarslan et al., 2006). These methods, collectively known as q-space imaging techniques, identify multiple fibers components by calculating the probability distribution function (PDF) of the diffusion process in each voxel based on the Fourier transform relationship between the PDF of diffusion displacement and the diffusion weighted signal attenuation in q-space. DSI performs a discrete Fourier transform to obtain $P(r,t)$, which requires a time intensive Cartesian sampling in q-space and hence is impractical for routine clinical use. QBI method takes measurements on a q-space ball and approximates the radial integral of the displacement probability distribution function by the spherical Funk-Radon transform. One problem with QBI is that the estimated diffusion orientation distribution function(ODF) is modulated by a zeroth-order Bessel function that induces spectral broadening of the diffusion peaks. DOT computes PDF at a fixed radius by expressing the Fourier transform in spherical coordinates and evaluating the radial part of the integral analytically assuming signals decay can be described by either a mono or a multi-exponential model. Özarslan et al. show that PDF values on a fixed radius can be reconstructed either directly or parametrically in terms of a Laplace series and claim that their technique can be regarded as a transformation of diffusivity to probability profiles whose peaks correspond to distinct fiber orientations. When signals decay is assumed is described by multi-exponential model, this technique requires data acquisition over multiple concentric spheres, a time consuming proposition.

An important limitation of q-space imaging techniques is that they do not enforce the estimated ODF to be non-negative; which can cause the estimated ODF to have negative values, a situation that does not obey the underlying principle of diffusion.

To overcome this limitation, Goh et al. proposed the use of spherical harmonic representation to pose the ODF estimation problem as a convex optimization problem and minimizing the cost function with coordinate descent method (Goh et al., 2009). While the authors claim that their method results to sharp diffusion ODFs, constrains the estimated ODF to be non-negative, and constrains the estimated ODF to be proper PDF (sum up to one); it remains to be seen how this method may be extended to multiple q-shell reconstruction method such as the one proposed in (Aganj et al., 2010). Similarly, Tournier et al. (Tournier et al., 2004, 2007) proposed constrained spherical deconvolution method to directly estimate the fiber orientation distribution (FOD) from Diffusion-Weighted MRI data and reduced the occurrence of negative values, albeit not completely eliminating them.

Of course, a careful distinction needs to be made between the two different concepts of diffusion ODF and fiber FOD functions although both have similar acronyms and are sometimes used interchangeably in DT-MRI research community. While q-space imaging techniques model the diffusion ODF, which is the radial marginal distribution of the diffusion PDF or ensemble average propagator (EAP) which in turn is the Fourier Transform of the diffusion signal; the technique by Tournier et al. (Tournier et al., 2004, 2007) models FOD based on deconvolution of a diffusion signal with a response function. ODF model holds true only when the signal is acquired using short gradient pulse assumption and it does not really indicate fiber orientations but rather the primary diffusion orientations. Moreover, ODF is known to have broad peaks partially due to the modulation of the Bessel function which is a concept from the q-space formalism that establishes the Fourier relationship between the diffusion signal and the diffusion PDF. The FOD on the other hand is a deconvolution of diffusion signal with a response function that indicates fiber orientations and needs to make no assumptions such as the narrow gradient pulse in the acquisition process and neither does it require a Fourier relationship between the diffusion signal and the diffusion PDF. Our method is therefore an extension the de-convolution definition (Tournier et al., 2004) and not the ODF (Tuch, 2004).

Another approach for multi-fiber reconstruction is to describe the apparent diffusion coefficient (ADC) by higher order diffusion tensors (e.g. 4^{th} and 6^{th}) that generalize the 2^{nd} order tensors and have the ability to approximate multi-lobed functions (Ozarslan and Mareci, 2003). Several methods have been proposed for estimating 4^{th} order tensors with positive semi-definite constraints (Barmpoutis et al., 2009; Barmpoutis and Vemuri, 2010; Ghosh et al., 2009) as well as for processing higher order tensor fields (Yassine and McGraw, 2009). This approach is attractive not only because the rich set of processing and analysis algorithms developed for second order tensor fields can be extended for higher order tensors, but also the local maxima of higher order tensors can be easily computed due to their simple polynomial form. The polynomial form of spherical functions represented as higher order tensors gives a significant algorithmic benefit from using the polynomial representations to compute the local maxima and minima compared to the equivalent spherical harmonics basis that need techniques such as finite difference method, spherical Newtons

method or Powells method. With the exception of the finite difference method, whose accuracy is limited to the mesh size, these methods are numerical minimization problems and thus care must be taken to avoid small local maxima and to ensure convergence (Bloy and Verma, 2008; Schultz and Seidel, 2008; Ghosh et al., 2011). Unfortunately, the use of higher order diffusion tensors has been confined to the estimation of tensor ADC profiles, although the local maxima of ADC profiles estimated using higher order tensors generally do not match the underlying fiber bundle orientations for the intravoxel crossing fibers (Alexander et al., 2002; Von dem Hagen and Henkelman, 2002; Zhan et al., 2004).

In this paper, we extend our previous work (Weldeselassie et al., 2010) where we developed the use of higher order symmetric positive semi-definite (PSD) Cartesian tensors to model FOD profiles and presented a novel method for estimating the tensor field of FOD profiles from a given set of DW-MR images. In our technique the FOD is modeled by Cartesian tensor basis using a parametrization that explicitly enforces the positive semi-definite property to the computed FOD functions. The computed Cartesian tensor FODs (CT-FODs) are PSD tensors whose coefficients can be efficiently estimated by solving a linear system with non-negative constraints. We evaluate our method qualitatively and quantitatively to demonstrate the superiority of the proposed technique over several existing multi-fiber reconstruction methods. Moreover, we use a distance measure for higher order tensors in order to derive diffusion anisotropy index computed directly from CT-FODs.

There are three main contributions in this paper:

- We present a novel method for positive semi-definite CT-FOD estimation from DW-MR images. To the best of our knowledge there is no existing FOD model in literature that imposes explicitly the positivity property to the estimated FOD, which is naturally a positive-valued spherical function.

- We present a useful application of our method for converting higher-order diffusion tensor ADC profiles to CT-FODs. We should emphasize that this is an essential task since the maxima of higher-order tensors do not correspond to the underlying fiber orientations. On the other hand, our method computes Cartesian Tensor FODs whose maxima can be computed analytically and correspond to the true diffusion orientations.

- We derive a rotationally invariant anisotropy index with range [0,1) defined directly on CT-FODs which consolidates the whole analysis pipeline of diffusion imaging using solely CT-FODs.

In addition to these features of the proposed method, our preliminary work (Weldeselassie et al., 2010) has also been recently extended by Jiao et al. (Jiao et al., 2011) where the authors not only demonstrated that the proposed CT-FOD model accurately detects crossings in white matter fibers but also estimating positive semi-definite fourth order tensor FODs can be achieved by minimizing an objective function subject to linear constraints by solving a linear programming problem that enforces non-negativity to computed ODFs.

2. Method

2.1. Symmetric Positive Semi-Definite Cartesian Tensors of Even Orders

Any spherical function $f(\mathbf{g})$ can be approximated by $L-th$ order Cartesian tensor as:

$$f(\mathbf{g}) \approx \sum_{i_1=1}^{3}\sum_{i_2=1}^{3}\cdots\sum_{i_L=1}^{3} g_{i_1}g_{i_2}\cdots g_{i_L}\mathbf{C}_{i_1,i_2,\cdots,i_L} \tag{2}$$

where g_i is the $i-th$ component of the 3-dimensional unit vector $\mathbf{g}$, and $\mathbf{C}_{i_1,i_2,\cdots,i_L}$ are the coefficients of an $L-th$ order tensor.

When approximating certain spherical functions in DT-MRI, we are interested in tensors of even orders with full symmetry, due to the antipodal symmetric nature of the DW-MR signal acquisition. In this case of symmetry, those tensor coefficients which correspond to the same monomial $g_1^a g_2^b g_3^c$ are equal to each other (e.g. $\mathbf{C}_{2,2,2,1} = \mathbf{C}_{2,2,1,2} = \mathbf{C}_{2,1,2,2} = \mathbf{C}_{1,2,2,2}$, since they all correspond to the monomial $g_1 g_2^3$).

Notation:- *The Einstein's notation of $L-th$ order tensors as $C_{i_1,i_2,\cdots,i_L}$ has been commonly used in literature. But in this notation, one needs to explicitly specify the constraints of symmetry as in the case of $C_{2,2,2,1} = C_{2,2,1,2} = C_{2,1,2,2} =$*

$C_{1,2,2,2}$ *above. In order to avoid such explicit specification of symmetry constraints, we will adopt an alternative notation that incorporates such symmetry constraints more naturally. In this new notation, the coefficient of a* $L-th$ *order tensor corresponding to the monomial* $g_1^i g_2^j g_3^k$ *is denoted by a single term* $C_{i,j,k}$ *with* $i+j+k=L$ *and the spherical function in Eq. 2 can more naturally be written as:*

$$f(\mathbf{g}) \approx \sum_{i+j+k=L} g_1^i g_2^j g_3^k \mathbf{C}_{i,j,k} \qquad i,j,k \in \{0,1,...,L\} \tag{3}$$

Using this alternative notation, the fifteen unique coefficients of fourth order PSD tensors are $\boldsymbol{C}_{400}$, $\boldsymbol{C}_{310}$, $\boldsymbol{C}_{301}$, $\boldsymbol{C}_{220}$, $\boldsymbol{C}_{211}$, $\boldsymbol{C}_{202}$, $\boldsymbol{C}_{130}$, $\boldsymbol{C}_{121}$, $\boldsymbol{C}_{112}$, $\boldsymbol{C}_{103}$, $\boldsymbol{C}_{040}$, $\boldsymbol{C}_{031}$, $\boldsymbol{C}_{022}$, $\boldsymbol{C}_{013}$, *and* $\boldsymbol{C}_{004}$. *Their corresponding terms using Einstein's notation are* $\boldsymbol{C}_{1111}$, $\boldsymbol{C}_{1112}$, $\boldsymbol{C}_{1113}$, $\boldsymbol{C}_{1122}$, $\boldsymbol{C}_{1123}$, $\boldsymbol{C}_{1133}$, $\boldsymbol{C}_{1222}$, $\boldsymbol{C}_{1223}$, $\boldsymbol{C}_{1233}$, $\boldsymbol{C}_{1333}$, $\boldsymbol{C}_{2222}$, $\boldsymbol{C}_{2223}$, $\boldsymbol{C}_{2233}$, $\boldsymbol{C}_{2333}$, *and* $\boldsymbol{C}_{3333}$ *respectively. More importantly, note the correspondence that* $\boldsymbol{C}_{i,j,k} = 4!/(i!\,j!\,k!)C_{i_1,i_2,\cdots,i_L}$. *Example* $\boldsymbol{C}_{400} = \boldsymbol{C}_{xxxx}$ *but that* $\boldsymbol{C}_{130} = 4\boldsymbol{C}_{xyyy}$ *etc.*

Furthermore, if the approximated function $f(\mathbf{g})$ is a positive-valued function, the Cartesian tensor should be positive-definite, i.e. $f(\mathbf{g}) > 0 \;\forall\; \mathbf{g} \in S_2$. Therefore Eq. 3 needs to be re-parametrized such that this positivity property is adhered to. In order to achieve this goal, we use the higher-order positive semi-definite tensor parametrization that has been recently proposed in (Barmpoutis and Vemuri, 2010) and theoretically justified in (Barmpoutis et al., 2012). According to this parametrization, any non-negative spherical function can be approximated by a positive semi-definite L^{th} order homogeneous polynomial in 3 variables expressed as a sum of squares of $(L/2)^{th}$ order homogeneous polynomials $p(g_1, g_2, g_3; \mathbf{u})$, where $\mathbf{u}$ is a vector that contains the polynomial coefficients.

$$f(\mathbf{g}) = \sum_{j=1}^{M} \lambda_j p(g_1, g_2, g_3; \mathbf{u}_j)^2 \tag{4}$$

The parameters λ_j in Eq. 4 are non-negative weights. This parametrization approximates any given symmetric positive function and the approximation accuracy depends on the order L and on how well the set of vectors $\mathbf{u}_j$ sample the space of unit vectors $\mathbf{u}$. It has been shown that by constructing a large enough set of well sampled vectors $\mathbf{u}_j$, we can achieve any desired level of accuracy (Barmpoutis and Vemuri, 2010; Barmpoutis et al., 2012).

2.2. Positive Semi-Definite Cartesian Tensor FOD (CT-FOD) Profiles

The DW-MR signal for a given magnetic gradient orientation $\mathbf{g}$ and gradient weighting b, can be modeled using the standard multi-fiber reconstruction framework as follows

$$S(\mathbf{g}, b) = \int_{S_2} w(\mathbf{v}) B(\mathbf{v}, \mathbf{g}, b) d\mathbf{v} \tag{5}$$

where the integration is over all unit vectors $\mathbf{v}$, $B(\mathbf{v}, \mathbf{g}, b)$ is a basis function, and $w(\mathbf{v})$ is a non-negative spherical function that can be seen as a mixing/weighting function. There have been several proposed models for the basis function $B()$ such as a Rigaut-type function (Jian et al., 2007), von Mises-Fisher distribution (Kumar et al., 2008) and others. The main problem with all of these models is that the integral in Eq. 5 cannot be computed analytically. Therefore, one needs to approximate the space of unit vectors $\mathbf{v}$ by a discrete set of vectors $\mathbf{v}_1, \cdots, \mathbf{v}_K$ in which case Eq. 5 is correctly discretized by $S(\mathbf{g}, b) = \sum_{k=1}^{K} w_k B(\mathbf{v}_k, \mathbf{g}, b)$ if and only if there are at most K underlying neural fibers that are oriented necessarily along the vectors $\mathbf{v}_k$. Another problem with the aforementioned discretization is that the function $w()$ is no more continuous over the sphere (it equals to w_k for $\mathbf{v}_k$ and it is zero everywhere else).

The main idea in this paper is to avoid the above unnatural discretization of the space of orientations, by using a blending function $w()$, which can be appropriately decomposed so that:

1. $w()$ is positive semi-definite, and
2. $w()$ is continuous over the sphere.

In this work, we model such blending function as a L^{th} order PSD tensor (say 4^{th}) by plugging Eq. 4 into Eq. 5 as follows

$$S(\mathbf{g}, b) = \int_{S_2} \sum_{j=1}^{M} \lambda_j p(v_1, v_2, v_3; \mathbf{u}_j)^2 B(\mathbf{v}, \mathbf{g}, b) d\mathbf{v} \tag{6}$$

where v_1, v_2, v_3 are the three components of the unit vector $\mathbf{v}$.

Given a data set of DW-MR signal attenuations S_i/S_0 associated with magnetic gradient orientations $\mathbf{g_i}$ and diffusion weighting b-value b, the coefficients of a L^{th} order positive semi-definite CT-FOD can be estimated by minimizing the following energy function with respect to the unknown polynomial-weighting coefficients λ_j

$$E = \sum_{i=1}^{N} \left(S_i/S_0 - \sum_{j=1}^{M} \lambda_j \int_{S_2} p(v_1, v_2, v_3; \mathbf{u}_j)^2 B(\mathbf{v}, \mathbf{g}_i, b) d\mathbf{v} \right)^2 \tag{7}$$

In order for the basis function $B()$ to reflect the signal attenuation of a single and highly oriented fiber response, we require the basis function to be a Gaussian that represents the diffusion process which is highly restricted perpendicular to the orientation $\mathbf{v}$. A common choice is the single fiber response which is described by the bipolar Watson function (Cook et al., 2004)

$$B(\mathbf{v}, \mathbf{g}, b) = \lim_{\delta \to +\infty} e^{-\delta(\mathbf{v}^T \mathbf{g})^2} \tag{8}$$

Here we should emphasize that the model in Eq. 8 agrees with the properties of the DW-MR signal response, i.e. it takes maximum and minimum values for diffusion sensitizing gradient orientations $\mathbf{g}$ that are perpendicular and parallel to the underlying fiber orientation $\mathbf{v}$ respectively. Moreover, $\delta = cb$ where c is a positive scalar captures information about b and mean diffusivity and can be adjusted by altering either b or c. So this 'symmetry' can be simplified by using only δ in Eq. 8. In computer implementation, due to finite precision calculations, Eq. 8 can be well approximated by setting delta to a very large constant.

In order to compute the CT-FOD, we need to solve the minimization problem Eq. 7 for $\lambda_j's$. This problem can be rewritten into an equivalent linear system problem $\mathbf{Bx = y}$ where $\mathbf{x}$ is an M-dimensional vector of the unknown λ_j, $\mathbf{y}$ is an N-dimensional vector containing the given signal attenuations S/S_i and $\mathbf{B}$ is a matrix of size $N \times M$ with the elements $\mathbf{B}_{i,j} = \int_{S_2} p(v_1, v_2, v_3; \mathbf{u}_j)^2 B(\mathbf{v}, \mathbf{g}_i, b) d\mathbf{v}$. This linear system is solved for the non-negative $\mathbf{x}$ using the efficient non-negative least squares (NNLS) algorithm given in (Lawson and Hanson, 1995). We can then easily compute the CT-FOD coefficients by multiplying the solution vector with a matrix $\mathbf{U}$, (i.e. $\mathbf{Ux}$), where the matrix $\mathbf{U}$ is of size $\frac{(2+L)!}{2(L!)} \times M$ that contains monomials formed by the vectors $\mathbf{u}_j$. Note that L is the order of the CT-FOD and $\frac{(2+L)!}{2(L!)}$ is the number of the unique coefficients in an L^{th}-order Cartesian tensor. In the case of 4^{th}-order CT-FODs, the multiplication $\mathbf{Ux}$ gives the 15 unique coefficients of a positive semi-definite tensor.

An interesting property of the NNLS optimization algorithm is that it produces sparse solution vectors and the sparsity depends on the rank of the basis matrix. In our particular case, although the problem seems significantly unconstrained; the solution vector contains at most as many non-zero weights as the unknown tensor coefficients, which corresponds to the rank of our polynomial basis matrix. Therefore if the finitely-generated set of polynomial basis contains a few thousands bases, the NNLS algorithm by definition will select only up to 6, 15, 28 for tensors of order 2, 4, and 6 respectively. Moreover the number of non-zero weights in the solution vector equals to the number of the unique unknown parameters of the symmetric tensor in each case. The sparsity of NNLS in comparison with other optimization techniques for modeling the diffusion-weighted MR signal has also been studied in (Jian and Vemuri, 2007). Therefore the degrees of freedom of our method is equal to the number of unknown tensor coefficients and it does not increase by the number of polynomial basis M but by the number of the unknown tensor coefficients.

We applied our proposed method for estimating 4^{th}-order CT-FODs ($L = 4$), using a set of $M = 321$ polynomial coefficients $\mathbf{u}_j$ and $\delta = 200$. Regarding the parameter δ, we performed several experiments using different values $\delta > 100$ and we obtained similar fiber orientations density profiles, which shows that our method is not sensitive to the selection of the value of δ.

2.3. Computing CT-FOD from higher-order Diffusion Tensor

Now, we present an application of our proposed framework for computing the coefficients of a CT-FOD from a given higher-order diffusion tensor and diffusion weighting b-value b, which is an essential task since the maxima of higher-order tensors do not correspond to the underlying fiber orientations. Given a higher-order diffusion tensor, the coefficients of the corresponding CT-FOD are computed by using the technique we presented in the previous section as follows

$$\mathbf{UB}^{-1} exp(-b\mathbf{Gt}) \tag{9}$$

where the matrices $\mathbf{U}$ and $\mathbf{B}$ are as defined in the previous section, $\mathbf{G}$ is of size $N \times \frac{(2+L)!}{2(L!)}$ and contains only monomials constructed from N unit vectors $\mathbf{g}_i$ uniformly distributed on the unit sphere, and $\mathbf{t}$ is a vector of size $\frac{(2+L)!}{2(L!)}$ that contains the unique coefficients of the given higher-order diffusion tensor. For example, in the case of 4^{th}-order tensors, the 15 unique coefficients are given in the vector $\mathbf{t}$, and $\mathbf{G}$ is of size $N \times 15$. Also notice that $\mathbf{B}$ is not a square matrix and the matrix inverse $\mathbf{B^{-1}}$ corresponds to the solution provided by the NNLS algorithm and therefore is a specifically non-negative constrained solution, in contrast to the general pseudo-inverse solution.

3. Distance and Anisotropy measures of CT-FOD

3.1. Distance Measure

After estimating CT-FODs, it is important that we define a distance measure between pairs of CT-FODs, for example, in order to impose smoothness across image lattice or to compute anisotropy measures. Since our CT-FODs are modeled as higher order (say 4^{th} order) PSD tensors which are isomorphic to homogeneous polynomial functions of same order, one way to get a distance measure between CT-FODs $\mathbf{C}_i$ and $\mathbf{C}_j$ is to define the distance as the L_2 distance between the corresponding spherical functions $f_i(\mathbf{g})$ and $f_j(\mathbf{g})$ as follows:

$$d^2(\mathbf{C}_i, \mathbf{C}_j) = \frac{1}{4\pi} \int_{S_2} (f_i(\mathbf{g}) - f_j(\mathbf{g}))^2 dg \tag{10}$$

where $f_i(\mathbf{g})$ and $f_j(\mathbf{g})$ are defined as given in Eq. 3 and the integral is over all unit vectors $\mathbf{g}$, i.e., the unit sphere S_2.

Observe that this distance measure has the same mathematical form as the tensor distance measure defined between higher order tensors in (Barmpoutis et al., 2009) when $f_i(\mathbf{g})$ and $f_j(\mathbf{g})$ are substituted with diffusivity functions. Denoting the fifteen components of $C_i - C_j$ by Δ_{xyz}, we get

$$\begin{aligned} d^2(\mathbf{C}_i, \mathbf{C}_j) = \frac{1}{315} \quad & \Big[(\Delta_{400} + \Delta_{040} + \Delta_{004} + \Delta_{220} + \Delta_{022} + \Delta_{202})^2 + \\ & 4[(\Delta_{400} + \Delta_{220})^2 + (\Delta_{400} + \Delta_{202})^2 + (\Delta_{040} + \Delta_{220})^2 + \\ & (\Delta_{040} + \Delta_{022})^2 + (\Delta_{004} + \Delta_{022})^2 + (\Delta_{004} + \Delta_{202})^2] + \\ & 24(\Delta_{400}^2 + \Delta_{040}^2 + \Delta_{004}^2) - 6(\Delta_{220}^2 + \Delta_{022}^2 + \Delta_{202}^2) + \\ & 2(\Delta_{400} + \Delta_{040} + \Delta_{004})^2 + (\Delta_{211} + \Delta_{031} + \Delta_{013})^2 + \\ & (\Delta_{121} + \Delta_{301} + \Delta_{103})^2 + (\Delta_{112} + \Delta_{310} + \Delta_{130})^2 + \\ & 2[(\Delta_{310} + \Delta_{130})^2 + (\Delta_{301} + \Delta_{103})^2 + (\Delta_{031} + \Delta_{013})^2] + \\ & 2(\Delta_{310}^2 + \Delta_{301}^2 + \Delta_{130}^2 + \Delta_{031}^2 + \Delta_{103}^2 + \Delta_{013}^2)\Big] \end{aligned} \tag{11}$$

3.2. Closest Isotropy

Given a CT-FOD $\mathbf{C}$, its closest isotropic CT-FOD $\mathbf{C}_{iso}$ is defined such that the distance $d(\mathbf{C}, \mathbf{C}_{iso})$ is minimum among all isotropic CT-FODs. The conditions for isotropy in the case of fourth order CT-FOD is:

$$\mathbf{C}_{iso} = \bar{\lambda}\, \mathbf{I}^s \tag{12}$$

for some $\bar{\lambda} \in \mathbb{R}^+$ and where $\mathbf{I}^s$ is a totally symmetric fourth order identity tensor (Moakher, 2008). In terms of components, $\mathbf{I}^s$ is given by

$$\begin{aligned} \mathbf{I}^s{}_{400} = \mathbf{I}^s{}_{040} = \mathbf{I}^s{}_{004} = 1 \\ \mathbf{I}^s{}_{220} = \mathbf{I}^s{}_{202} = \mathbf{I}^s{}_{022} = 2 \end{aligned} \tag{13}$$

and all remaining components equal to zero. Using this result and minimizing the distance $d(\mathbf{C}, \mathbf{C}_{iso})$ with respect to $\bar{\lambda}$, we obtain (Moakher and Norris, 2006)

$$\bar{\lambda} = \frac{1}{5}(\mathbf{C}_{400} + \mathbf{C}_{040} + \mathbf{C}_{004}) + \frac{1}{15}(\mathbf{C}_{220} + \mathbf{C}_{202} + \mathbf{C}_{022}) \tag{14}$$

Observe that $\bar{\lambda}$ is actually the mean FOD of the CT-FOD $\mathbf{C}$ which is the same as saying the zeroth order CT-FOD that is closest to $\mathbf{C}$.

3.3. Anisotropy Measure

We now present an anisotropy measure derived from fourth order CT-FODs. This is important in order to consolidate the work of diffusion tensor imaging towards CT-FODs. Similar to the definition of fractional anisotropy (FA) for second order tensors, we propose the use of the distance of a given a CT-FOD from its closest isotropy normalized by the norm of the CT-FOD as our anisotropy index. Defining the norm of a given CT-FOD as its $L2$ distance from **ZERO**, we see that the non-negative function $d(\mathbf{C}, \mathbf{C}_{iso})/d(\mathbf{C}, \mathbf{0})$ can be used to infer anisotropy index. It is easy to see that this expression takes its minimum value of 0 when $\mathbf{C}$ is isotropic. In order to find its upper bound, it suffices to look at the limiting, but physically impossible, case of a non-zero diffusivity in only one direction, say along the direction $\mathbf{v} = (1, 0, 0)^T$ but zero diffusivities along all directions perpendicular to $\mathbf{v}$. In this case, all components of C except $\mathbf{C}_{400}$ will be zero and its mean FOD will be $\mathbf{C}_{400}/5$ resulting an upper bound of $4/5$. In order to have an anisotropy index in the range $[0, 1)$, we would like to find a monotonic function that will map the interval $[0, \frac{4}{5})$ to $[0, 1)$. While several mapping functions can achieve this, in this work we choose a linear mapping and define our anisotropy measure as

$$AI = \frac{5}{4}\left(\frac{d(\mathbf{C}, \mathbf{C}_{iso})}{d(\mathbf{C}, \mathbf{0})}\right) \tag{15}$$

We simulated several synthetic diffusion profiles comprising of isotropic, planar, linear and crossing fibers profiles in order to to see the behavior of this anisotropy measure and compare it with existing measures. Fig. 1, shows

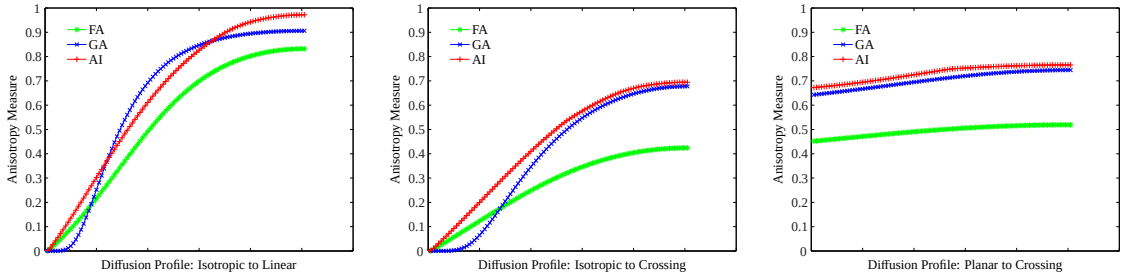

Figure 1: Comparison of FA, GA and our AI as diffusion profiles range from isotropic to linear (*left*), isotropic to two perpendicular crossing fibers (*middle*), and planar to two crossing fibers on the plane (*right*).

anisotropy measures as obtained by our anisotropy index, FA and generalized anisotropy (GA) as defined in (Ozarslan et al., 2005). The DW signals for these simulations were generated using the realistic diffusion MR simulation model proposed in (Söderman and Jönsson, 1995). For the case of isotropic to linear diffusion profile (Fig. 1 *left*), we started with 321 crossing fiber orientations that uniformly sample the unit hemisphere with equal diffusivities and then gradually (*in 100 time steps*) restricted the diffusion in all directions but along one fiber orientation. In this configuration, while both FA and our anisotropy measures show monotonically increasing values as we move from isotropic to linear diffusion, GA however shows little changes at both isotropic and anisotropic regions with larger changes in the intermediate regions. As a result while the contrast of GA is concentrated in the gray matter, the contrast in both FA and our anisotropy measures is more or less uniform at all regions. Similarly, for the case of isotropic to two crossing fibers (Fig. 1 *middle*), we started with the same 321 fiber orientations with equal diffusivities and then gradually restricted diffusion in all directions but two perpendicular fiber orientations. The important observation in this case is the fact that both GA and our anisotropy measure give rise to larger values for crossing fibers while FA does not, which highlights the limitation of second order tensor model in crossing fibers regions. Finally in the case

of planar to two crossing fibers (Fig. 1 *right*), we started with 16 crossing fiber orientations on a plane that sample a circle uniformly and then restricted diffusion in all but two perpendicular directions on the plane. As expected not only does FA gave rise to more or less uniform values in this configuration, but surprisingly both GA and our anisotropy measures did so too, albeit with higher values. In other words, even though both fourth order tensor ADC and FOD models are able to model two crossing fibers, they do not distinguish as such between only two or more than two crossing fibers. This is of course the limitation of 4^{th} order tensor model when there are more than two crossing fibers. From tractography point of view, where anisotropy index is used for seeding and stopping criteria, however unlike FA both GA and our anisotropy measure will be good indicators of presence of fibrous structures because they show high anisotropy value in such regions (close to 0.7).

4. Experimental Results

In this section, we present experimental results of the proposed method applied to simulated as well as real DW-MR image from a human brain dataset.

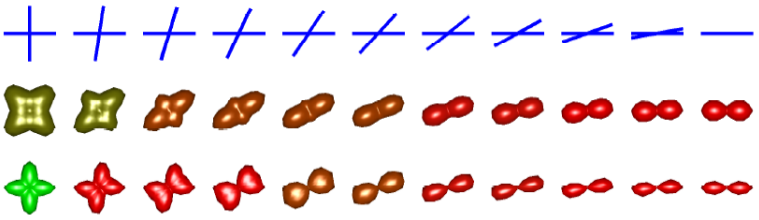

(a) Noise free. Top to bottom: schematic diagram of orientations, ADC profiles and FOD profiles.

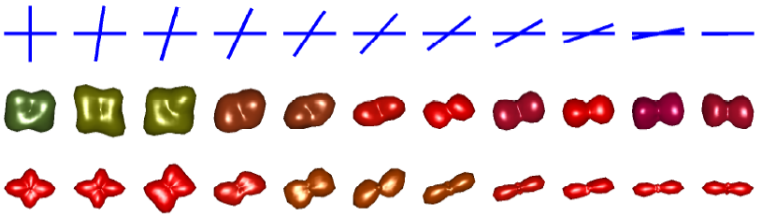

(b) Rician noise, std. dev.=0.02. Top to bottom: schematic diagram of orientations, ADC profiles and FOD profiles.

Figure 2: Alignment of maxima of estimated ADC and CT-FOD profiles with underlying fiber orientations.

4.1. Synthetic Dataset

In order to highlight the accuracy with which the maxima of estimated CT-FOD profiles coincide with the actual underlying fiber orientations, we first present qualitative results for the case of a synthetic dataset comprising of two crossing fiber bundles modeled as fourth order CT-FODs as shown in Fig. 2. Included is also the results of ADC profiles modeled as fourth order tensors in order to highlight the performance of CT-FODs over ADC tensors of same order. In this experiment, we start with two fiber bundles crossing at 90° degrees and then rotate one of the fiber orientations gradually until it aligns with the second fiber orientation resulting to a single fiber. The DW-MR signals for this simulated experiment were generated by simulating the MR signals using the realistic diffusion MR simulation model in (Söderman and Jönsson, 1995) with $b\text{-}value = 1500 s/mm^2$ and 81 gradient directions. Fig. 2(a) shows the result for a noise free case and Fig. 2(b) shows the results obtained when a Rician noise with std. dev. = 0.02 is added to the simulated DW-MR signals. It is evident from these results that not only do CT-FOD profiles model the underlying structure better but also have better noise immunity.

Next, we present quantitative results by presenting the deviation angles of the maxima of estimated CT-FODs with respect to the actual underlying fiber orientations. We consider the case of two crossing fibers whose orientations are

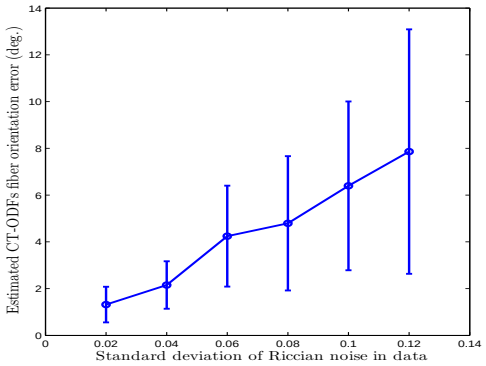

Table of errors (deg.)
noise st. dev. = 0.08

Method	Mean	St. dev.
QBI	9.125	±4.545
DOT	6.645	±3.720
MOVMF	5.624	±3.514
MOW	5.010	±2.955
CT-FOD	4.793	±2.873

Figure 3: Deviation angle between actual fiber orientations and maxima of estimated CT-FODs using a simulated 2-fiber crossing data with orientations ($\cos 20°,\ \sin 20°,\ 0$) and ($\cos 100°,\ \sin 100°,\ 0$) at different levels of Rician noise.

($\cos 20°,\ \sin 20°,\ 0$) and ($\cos 100°,\ \sin 100°,\ 0$) and the DW-MR signals are generated as described above. In order to compare our results with spherical deconvolution techniques, we also include the results obtained using MOW (Jian et al., 2007), QBI (Tuch, 2004), DOT (Özarslan et al., 2006) and MOVMF (Kumar et al., 2008) methods by computing the maxima of either the PDF or FOD profiles of the corresponding methods. Six distinct Rician noise levels were added to the simulated data and for each noise level the experiments were repeated 100 times. Fig. 3 shows a plot of the means and standard deviations of deviation angles between the actual fiber orientations and the maxima of estimated CT-FODs. For the particular noise level with std. dev. = 0.08 the deviation angles for all the methods are reported in the adjacent table. Also notice that in this experiment the deviation angle of the computed orientations is compared to its closest actual fiber orientation because the crossing fibers are weighted equally in generating the MR signals. The results demonstrate the superiority of the proposed method over QBI, DOT, MOVMF and MOW methods.

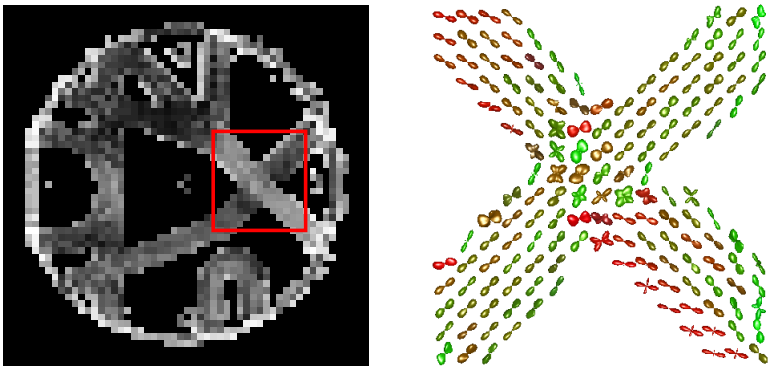

(a) Generalized anisotropy. (b) 4^{th}-order CT-FOD.

Figure 4: Generalized anisotropy and 4^{th}-order CT-FOD for fibercup phantom data. Crossing of fiber orientations is clearly depicted as expected.

4.2. Phantom Dataset

Here, we present our results for the publicly available HARDI phantom dataset whose ground truth fibers are known and was used in the MICCAI 2009 Fiber Cup contest (Poupon et al., 2008). The dataset consisted of 64 diffusion weighted images and one S_o volume acquired in two different spatial resolutions: $3x3x3mm^3$ and $6x6x6mm^3$ and three different b-values: 650,1500 and 2650 s/mm2. We used the $3x3x3mm^3$ resolution dataset with a b-value of 650s/mm2. Fig. 4(a) shows generalized anisotropy while Fig. 4(b) gives a zoomed in visualization of fourth order CT-

FODs computed for the box shown in red. Clearly the fourth order CT-FOD correctly depicts the fiber organization of crossings as well as single fiber orientations.

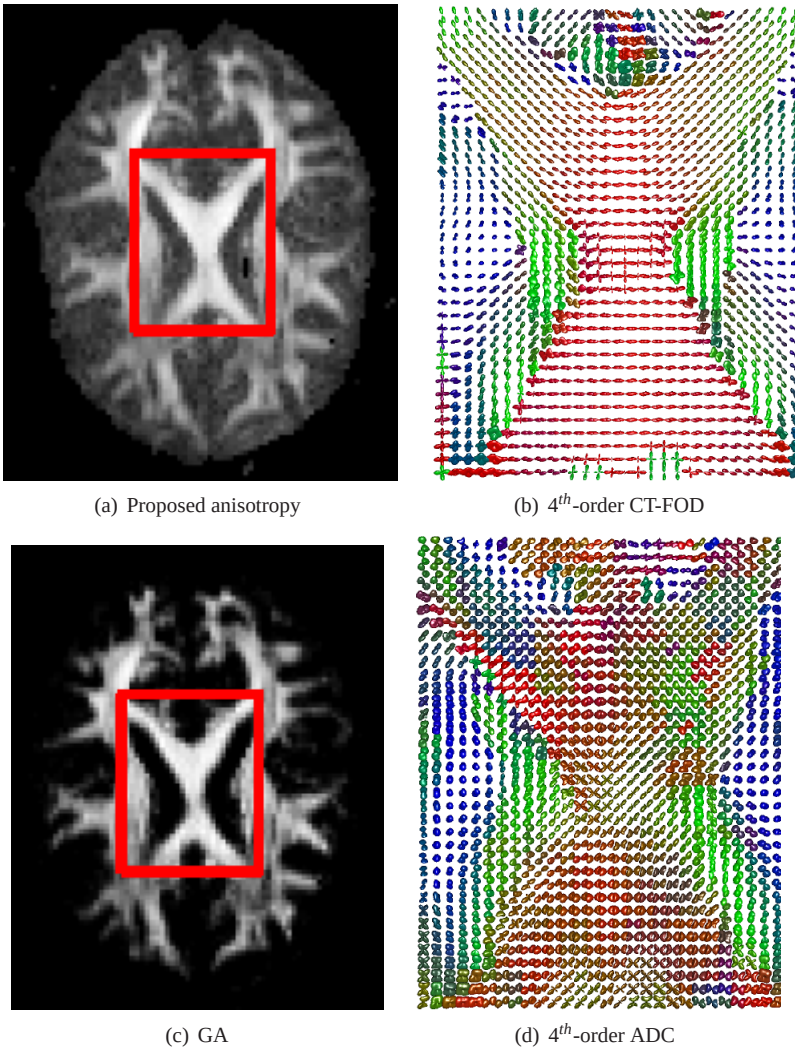

(a) Proposed anisotropy (b) 4^{th}-order CT-FOD

(c) GA (d) 4^{th}-order ADC

Figure 5: 4^{th}-order CT-FOD and ADC tensor fields computed from human brain slice and their corresponding anisotropy measures.

4.3. Real Dataset

Next, we present CT-FODs computed from a real dataset consisting of a human brain dataset. The dataset consists of 63 continuous slices of 2.0 *mm* thickness with a field of view (FOV) of $256 \times 256 mm^2$ and pixel size of $2 \times 2 mm^2$. 10 images were collected without diffusion weighting ($b \sim 0 s/mm^2$) which were averaged during the CT-FOD reconstruction for a single average S_o image and 99 diffusion weighted images are acquired in 99 gradient directions. Each of these image sets used different diffusion gradients with approximate b values of $3000 s/mm^2$. Fig. 5 shows fourth order CT-FODs computed using our method along with the proposed anisotropy index. Included is also fourth order diffusion tensors and generalized anisotropy images. As can be verified in the anisotropy images; the branching, bending and crossing of tracts are better depicted by the computed CT-FODs as compared to the diffusion tensors. Moreover unlike generalized anisotropy map which reveals the white matter region with higher contrast but fails to distinguish the gray matter from the background, the proposed anisotropy map reveals both white matter and gray matter regions more clearly, albeit with less contrast.

Based on our preliminary CT-FOD results (Weldeselassie et al., 2010) and in conjunction with their techniques, Jiao et al. (Jiao et al., 2011) have already shown that the proposed CT-FOD model improves tractography results and accurately detects fiber crossings, splits and kisses. Another potential fiber tracking algorithm that may be used in conjunction with CT-FOD is the spin glass based framework to untangle fiber crossing (Cointepas et al., 2002).

4.4. Tissue discrimination with GA and AI

Finally, we present a quantitative comparison of the anisotropy index derived from CT-FOD with generalized anisotropy in discriminating different tissue classes in a brain image. For the task of discriminating between two tissue classes, a measure of diffusion anisotropy, A, can be evaluated using a detectability index Alexander et al. (2000),

$$d = \frac{< A_1 > - < A_2 >}{\sqrt{\sigma_1^2 - \sigma_2^2}} \tag{16}$$

where ($< A_1 >$, σ_1^2) and ($< A_2 >$, σ_2^2) are the means and variances of the anisotropy values for the two tissue classes. The anisotropy measure with the greatest detectability index should be close to optimum for the specified task. In order to compare GA and AI in discriminating tissue classes, we calculated the detectability indices of these anisotropy measures for the dataset described in section 4.3 above. The brain was parcellated using a publicly available while matter parcellation map (JHU_MNI_SS_WMPM_TypeI) downloaded from Johns Hopkins Medical Institute Laboratory of Brain Anatomical MRI. The GA and AI maps of our dataset were registered to the white matter parcellation map using FA map that was came with the parcellation map and was already registered to it. An affine registration was performed using the DiffeoMap software downloaded from the same source. Figure 6 shows the publicly available FA map with five regions of interest segmented. Our tissue detectability results for the regions of interest are presented in Table 1 where the values of d shown in bold face indicate that the anisotropy index given on that row performs best in discriminating tissue classes on the corresponding column. We observe that our anisotropy index generally performs better in detecting differences among tissues presented.

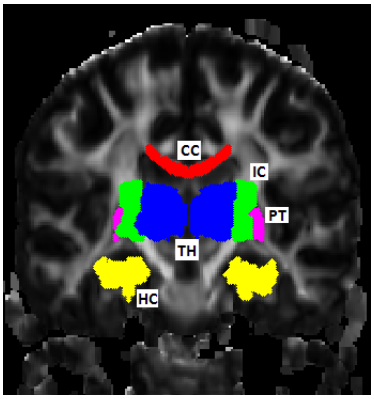

Figure 6: Single slice of FA map from JHU_MNI_SS DTI dataset with corresponding regions of interest segmented using JHU_MNI_SS_WMPM_TypeI white matter parcellation map: CC = Corpus Callosum, IC = Internal Capsule, TH = Thalamus, HC = Hippocampus, and PT = Putamen

Table 1: Tissue detectability using GA and AI

AI\ ROI	CC vs IC	CC vs TH	CC vs HC	CC vs PT	IC vs TH	IC vs HC	IC vs PT	TH vs HC	TH vs PT	HC vs PT
GA	0.6931	0.7361	0.5330	0.7686	**0.4210**	**0.2045**	0.5422	**0.3897**	0.3575	0.5578
AI	**0.8080**	**1.4826**	**0.7314**	**0.9621**	0.0938	0.1794	**0.5861**	0.0662	**0.4429**	**0.6329**

5. Conclusions

We presented a novel technique to estimate FODs modeled as PSD high order tensors from DW-MR images. The performance of the proposed method is compared against several existing FOD measures on a synthetic dataset with different noise levels and outperformed the other methods. We also demonstrated the use of our method on a real DT-MR image obtained from a human brain dataset. Our results clearly demonstrate the superiority with which the organizational structure of an underlying diffusion process is neatly modeled with CT-FODs as compared to higher order diffusion tensors and the fact that crossing, merging and bending of fibers are correctly depicted with CT-FODs. By deriving anisotropy map directly from CT-FOD profiles, we have attempted to consolidate the analysis of diffusion imaging towards the use of solely CT-FODs. Future work includes processing of diffusion images such as segmentation and registration tasks with the proposed CT-FOD fields.

6. Acknowledgment

We thank Jennifer Campbell research associate of the McConnell Brain Imaging Centre, Montreal Neurological Institute, McGill University for generously providing us the brain dataset used in this study. We also thank Johns Hopkins Medical Institute Laboratory of Brain Anatomical MRI and their grants 1 RO1 AG20012-01 / P41 RR15241-01A1 for making the brain white matter parcellation map and the DiffeoMap software available (http://lbam.med.jhmi.edu/). This research is partly funded by Canadian Natural Sciences and Engineering Research Council (NSERC). Last but not least we thank the anonymous reviewers who reviewed our first submission and recommended excellent suggestions.

7. Biographies

Prof. Barmpoutis' current research interests lie in the areas of machine vision and applications, virtual reality in medicine, human motion capture and analysis, biomedical image processing and visualization, and facial recognition and expression analysis. He has coauthored more than 40 journal and conference publications. Dr. Barmpoutis has received various awards and scholarships, including the Outstanding Academic Achievement Award from the College of Engineering, the CIEGL bursary from the University of Oxford, and the University of Florida Alumni Fellowship.

Prof. Atkins is a co-director of Medical Image Computing Analysis (MICA) lab at the School of Computing Science, Simon Fraser University. Her research interests span the areas of Diffusion Tensor Magnetic Resonance Imaging, Eye-gaze tracking in surgery applications, Telepathology , and Skin Cancer and Melanoma analysis using dermoscopic images. She has coauthored over 135 journal and conference publications. Dr. Atkins has received several research funding awards including Canadian Natural Sciences and Engineering Research Council (NSERC), Canadian Health Research Projects (CHRP), and NATO Science for Peace.

Yonas T. Weldeselassie is a Ph.D. candidate at the School of Computing Science, Simon Fraser University under the supervision of Dr. M. Stella Atkins. His research interests include analysis of Diffusion Tensor Magnetic Resonance (DT-MR) images, Statistical Modeling and Optimization. He has received several awards during his postgraduate studies including fellowship assistance at the Abdus Salam International Center for Theoretical Physics, Simon Fraser University Entrance Scholarship, MITACS Internship (Spring 2007, Summer 2007, Fall 2007, and Summer 2011), Simon Fraser University Graduate Fellowship (Spring 2008), and Simon Fraser University President's Stipend Graduate Fellowship (Spring 2011).

References

Aganj, I., Lenglet, C., Sapiro, G., Yacoub, E., Ugurbil, K., Harel, N., 2010. Reconstruction of the orientation distribution function in single-and multiple-shell q-ball imaging within constant solid angle. Magnetic Resonance in Medicine 64 (2), 554–566.

Alexander, A., Hasan, K., Kindlmann, G., Parker, D., Tsuruda, J., 2000. A geometric analysis of diffusion tensor measurements of the human brain. Magnetic Resonance in Medicine 44 (2), 283–291.

Alexander, D., Barker, G., Arridge, S., 2002. Detection and modeling of non-Gaussian apparent diffusion coefficient profiles in human brain data. Magnetic Resonance in Medicine 48 (2), 331–340.

Barmpoutis, A., Ho, J., Vemuri, B. C., In Press 2012. Approximating symmetric positive semi-definite tensors of even order. SIAM Journal on Imaging Sciences.

Barmpoutis, A., Hwang, M., Howland, D., Forder, J., Vemuri, B., 2009. Regularized positive-definite fourth order tensor field estimation from DW-MRI. Neuroimage 45 (1), 153–162.
Barmpoutis, A., Vemuri, B. C., 2010. A Unified Framework For Estimating Diffusion Tensors Of Any Order With Symmetric Positive-Definite Constraints. In: Proceedings of the 7th IEEE International Symposium on Biomedical Imaging: From Nano to Macro. pp. 1385–1388.
Bloy, L., Verma, R., 2008. On computing the underlying fiber directions from the diffusion orientation distribution function. In: Proceedings of Medical Image Computing and Computer-Assisted Intervention–MICCAI 2008. Springer, pp. 1–8.
Cointepas, Y., Poupon, C., Le Bihan, D., Mangin, J., 2002. A spin glass based framework to untangle fiber crossing in mr diffusion based tracking. Medical Image Computing and Computer Assisted Intervention (MICCAI 2002), 475–482.
Cook, P., Alexander, D., Parker, G., 2004. Modelling noise-induced fibre-orientation error in diffusion-tensor mri. In: IEEE International Symposium on Biomedical Imaging: Nano to Macro, 2004. IEEE, pp. 332–335.
Descoteaux, M., Angelino, E., Fitzgibbons, S., Deriche, R., 2006. A Fast And Robust ODF Estimation Algorithm In Q-Ball Imaging. In: Proceedings of the 3rd IEEE International Symposium on Biomedical Imaging: From Nano to Macro. pp. 81–84.
Descoteaux, M., Angelino, E., Fitzgibbons, S., Deriche, R., 2007. Regularized, fast, and robust analytical Q-ball imaging. Magnetic Resonance in Medicine 58 (3), 497–510.
Ghosh, A., Deriche, R., Moakher, M., 2009. Ternary Quartic Approach For Positive 4th Order Diffusion Tensors Revisited. In: Proceedings of the 6th IEEE International Symposium on Biomedical Imaging: From Nano to Macro. pp. 618–621.
Ghosh, A., Wassermann, D., Deriche, R., 2011. A polynomial approach for maxima extraction and its application to tractography in hardi. In: Information Processing in Medical Imaging. Springer, pp. 723–734.
Goh, A., Lenglet, C., Thompson, P., Vidal, R., 2009. Estimating orientation distribution functions with probability density constraints and spatial regularity. In: Proceedings of the 12th International Conference on Medical Image Computing and Computer Assisted Intervention (MICCAI 2009). Springer, pp. 877–885.
Jian, B., Vemuri, B., 2007. Multi-fiber reconstruction from diffusion mri using mixture of wisharts and sparse deconvolution. In: Proceedings of the 20th International Conference on Information Processing in Medical Imaging. Springer-Verlag, pp. 384–395.
Jian, B., Vemuri, B., Özarslan, E., Carney, P., Mareci, T., 2007. A novel tensor distribution model for the diffusion-weighted MR signal. NeuroImage 37 (1), 164–176.
Jiao, F., Gur, Y., Johnson, C., Joshi, S., 2011. Detection of Crossing White Matter Fibers with High-Order Tensors and Rank-k Decompositions. In: Proceedings of the 22nd International Conference on Information Processing in Medical Imaging, IPMI. Springer, pp. 538–549.
Kumar, R., Barmpoutis, A., Vemuri, B., Carney, P., Mareci, T., 2008. Multi-Fiber Reconstruction from DW-MRI using a Continuous Mixture of von Mises-Fisher Distributions. In: Proceedings of IEEE Computer Society Conference on Computer Vision and Pattern Recognition. pp. 1–8.
Lawson, C., Hanson, R., 1995. Solving Least Squares Problems, Chapter 23. Vol. 15. Society for Industrial and Applied Mathematics.
Moakher, M., 2008. Fourth-Order Cartesian Tensors: Old And New Facts, Notions And Applications. The Quarterly Journal of Mechanics and Applied Mathematics 61 (2), 181–203.
Moakher, M., Norris, A., 2006. The closest elastic tensor of arbitrary symmetry to an elasticity tensor of lower symmetry. Journal of Elasticity 85 (3), 215–263.
Ozarslan, E., Mareci, T., 2003. Generalized Diffusion Tensor Imaging and Analytical Relationships Between Diffusion Tensor Imaging and High Angular Resolution Diffusion Imaging. Magnetic Resonance in Medicine 50 (5), 955–965.
Özarslan, E., Shepherd, T., Vemuri, B., Blackband, S., Mareci, T., 2006. Resolution of complex tissue microarchitecture using the diffusion orientation transform (DOT). NeuroImage 31 (3), 1086–1103.
Ozarslan, E., Vemuri, B., Mareci, T., 2005. Generalized Scalar Measures for Diffusion MRI Using Trace, Variance, and Entropy. Magnetic Resonance in Medicine 53 (4), 866–876.
Poupon, C., Rieul, B., Kezele, I., Perrin, M., Poupon, F., Mangin, J., 2008. New diffusion phantoms dedicated to the study and validation of high-angular-resolution diffusion imaging (HARDI) models. Magnetic Resonance in Medicine 60 (6), 1276–1283.
Schultz, T., Seidel, H., 2008. Estimating Crossing Fibers: A Tensor Decomposition Approach. IEEE Transactions on Visualization and Computer Graphics (TVCG) 14 (6), 1635–1642.
Söderman, O., Jönsson, B., 1995. Restricted Diffusion in Cylindrical Geometry. Journal of Magnetic Resonance. Series A 117 (1), 94–97.
Tournier, J., Calamante, F., Connelly, A., 2007. Robust determination of the fibre orientation distribution in diffusion MRI: non-negativity constrained super-resolved spherical deconvolution. NeuroImage 35 (4), 1459–1472.
Tournier, J., Calamante, F., Gadian, D., Connelly, A., 2004. Direct estimation of the fiber orientation density function from diffusion-weighted mri data using spherical deconvolution. NeuroImage 23 (3), 1176–1185.
Tuch, D., 2004. Q-Ball Imaging. Magnetic Resonance in Medicine 52 (6), 1358–1372.
Tuch, D., Reese, T., Wiegell, M., Van J, W., 2003. Diffusion MRI of Complex Neural Architecture. Neuron 40 (5), 885–895.
Tuch, D., Weisskoff, R., Belliveau, J., Wedeen, V., 1999. High Angular Resolution Diffusion Imaging of the Human Brain. In: 7th Annual Meeting of International Society for Magnetic Resonance in Medicine. p. 321.
Von dem Hagen, E., Henkelman, R., 2002. Orientational Diffusion Reflects Fiber Structure Within a Voxel. Magnetic Resonance in Medicine 48 (3), 454–459.
Wedeen, V., Hagmann, P., Tseng, W., Reese, T., Weisskoff, R., 2005. Mapping Complex Tissue Architecture With Diffusion Spectrum Magnetic Resonance Imaging. Magnetic Resonance in Medicine 54 (6), 1377–1386.
Weldeselassie, Y., Barmpoutis, A., Atkins, M. S., 2010. Symmetric Positive-Definite Cartesian Tensor Orientation Distribution Functions (CT-ODF). In: Proceedings of the 13th International Conference on Medical Image Computing and Computer-Assisted Intervention: Part I. Springer-Verlag, pp. 582–589.
Yassine, I., McGraw, T., 2009. 4th Order Diffusion Tensor Interpolation with Divergence and Curl Constrained Bézier Patches. In: Proceedings of the 6th IEEE International Symposium on Biomedical Imaging: From Nano to Macro. pp. 634–637.
Zhan, W., Stein, E., Yang, Y., 2004. Mapping the orientation of intravoxel crossing fibers based on the phase information of diffusion circular spectrum. NeuroImage 23 (4), 1358–1369.